Journal Pre-proof

Corrosive wear of multi-layer Fe-based coatings laser cladded from amorphous powders

Xiulin Ji, Chanyuan Luo, Yong Sun, Jianhua Zhao

PII: S0043-1648(19)30647-7

DOI: https://doi.org/10.1016/j.wear.2019.203113

Reference: WEA 203113

To appear in: *Wear*

Received Date: 8 April 2019

Revised Date: 30 October 2019

Accepted Date: 1 November 2019

Please cite this article as: X. Ji, C. Luo, Y. Sun, J. Zhao, Corrosive wear of multi-layer Fe-based coatings laser cladded from amorphous powders, *Wear* (2019), doi: https://doi.org/10.1016/j.wear.2019.203113.

A coating with super corrosive wear resistance formed from amorphous powder

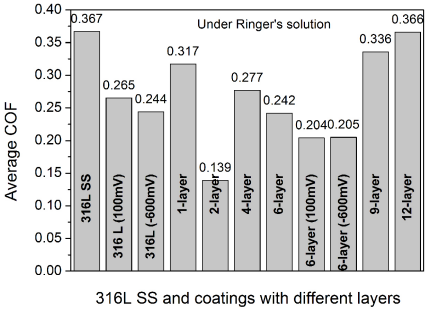

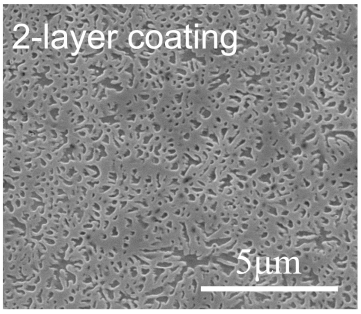

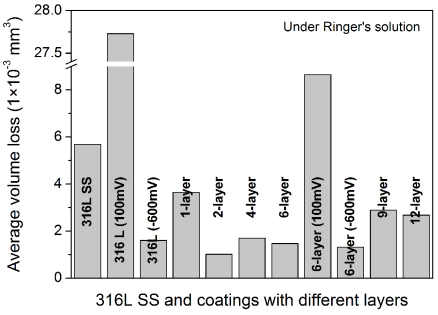

Corrosive wear of multi-layer Fe-based coatings laser cladded from amorphous powders

Xiulin Ji[1, 2, *], *Chanyuan Luo*[1], *Yong Sun*[3, *], *Jianhua Zhao*[1]

[1] Engineering Research Center of Dredging Technology of Ministry of Education, Hohai University, Changzhou 213022, China

[2] Department of Mechatronics Engineering, Shantou University, 515063, China

[3] School of Engineering and Sustainable Development, Faculty of Computing, Engineering and Media, De Montfort University, Leicester LE1 9BH, UK

Corresponding Author: xiulinji@gmail.com (X. Ji); ysun01@dmu.ac.uk (Y. Sun)

Key words: Corrosive wear; metal matrix composites; amorphous alloy; polarization; coatings; tribocorrosion

Abstract

Since amorphous alloys exhibit good wear and corrosion resistance, they are supposed to be applied as a candidate implant material. In this work, using laser cladding, Multi-layer Fe-based alloy coatings were fabricated from amorphous powders on 316L stainless steel (SS) substrate. When the number of cladding layers increases, the microstructure of the coating was mainly composed of γ-Fe firstly, then evolved to γ-Fe and α-Fe solid solutions, and then to a composite of amorphous and crystalline phases. The surface hardness of the coating was also enhanced consequently to over 1200 HV. During reciprocate sliding against an Alumina ball in a simulated body fluid (Ringer's solution), the volume loss and the coefficient of friction (COF) of the coatings generally decreased firstly and then increased with the number of cladding layers. During sliding at open circuit, the drop in open circuit potential (OCP) of all the Fe-based coatings, except for the 1-layer one, was not as significant as

that of the 316 SS substrate. Moreover, when applying a cathodic potential during sliding, no obvious protective effect was obtained for the coatings, which indicates that the multi-layer Fe-based coatings possess a good corrosion-induced wear resistance in comparison to 316L SS. Because of the formation of an electric double layer, the fixed potential of 100 mV_{SCE} or -600 mV_{SCE} was beneficial to reduce the COF, especially for 316L SS. The tribocorrosion at OCP showed that the 2-layer coating possessed the best corrosive wear resistance, and its COF and volume loss were about 3 and 5.6 times lower than those of the substrate. The material loss in Ringer's solution at OCP is mainly controlled by the mechanical wear for the coatings and the synergism between corrosion and wear for the substrate. Furthermore, this work provides a way to optimize the tribology system by adjusting the number of cladding layers to reduce COF and wear in a simulated body fluid.

1. Introduction

Total hip replacement (THR) has emerged as an efficient surgical procedure for relieving pain and restoring hip mobility [1], while the metallic based load bearing bio-implants are suffering corrosive wear which also causes health issues [2]. To enhance the durability of artificial joints, a plausible way is to generate a highly wear-resistant coating on the bearing surfaces [3]. Amorphous alloys (that is, metallic glasses) having a similar atom structure with that of liquids show better wear and corrosion resistance than crystallized alloys in most cases, and become the potential engineering alloys for anti-corrosive wear applications [4]. Amorphous metallic thin films show great promise for applications where mechanical and chemical attack coexist due to their excellent wear, corrosion, and tribocorrosion resistance [5]. Therefore, the amorphous alloys and their coatings without cytotoxic elements are promising biocompatible materials for bio-implant applications [6].

Normally, amorphous alloy coatings are prepared by thermal spraying, magnetron sputtering or electrodeposition [7-9]. Laser cladding [10-14] is another effective way to fabricate amorphous alloy coatings, especially for a metallurgical bonding. Since the formation of the amorphous phase is sensitive to chemical compositions, the components of the laser clad amorphous coatings should be restricted to a narrow range [11]. Some of the reported laser processing of Fe-based and other amorphous coatings involved two stage deposition processes, i.e. preplacing or depositing amorphous alloy on the substrates, and then remelting to obtain surface amorphization. Other methods involved direct deposition of amorphous alloy powder on crystalline substrates [12, 13]. Although the laser parameters were extensively studied, a complete amorphous microstructure deposited by laser cladding was still difficult for the open environment and the limited cooling rates. So the coating thickness normally is limited to 1.2 mm [14]. Except for the laser parameters, powder purity and shielding gas also have obvious influences on the glass-forming ability of alloy coatings. Moreover, because the chemical composition is very important to the glass-forming ability, and the dilution from the substrate can cause a chemical composition change. Thus, dilution is another important factor of consideration in

order to obtain the amorphous phase from laser cladding.

On the other hand, although corrosion and friction behavior of amorphous alloys and their coatings has been extensively studied during the past decade, there is limited work related to their tribocorrosion behavior [15]. In a 3.5% NaCl solution, the overall average friction coefficient of the Fe-based amorphous alloy was varied from 0.18 to 0.25 depending on the test conditions, and the wear resistance was better than that of the commercial bearing steel [4]. Our former work not only proved that the Zr-based amorphous alloy has better tribocorrosion resistance than that of AISI 304 stainless steel (SS), but also showed the amorphous alloy is beneficial to reduce the wear of the counterface (bearing steel disk) [16]. Similarly, because of the highly hydrophilic surfaces in sterile calf bovine serum and Hank's solution, Zr-based amorphous alloy decreased the wear rate of the counterface (ultra-high-molecular-weight polyethylene, UHMWPE) over 20 times lower than that caused by conventional cast CoCrMo alloy [17]. Unfortunately, there are still some challenges in the application of amorphous alloys in tribocorrosion. In some conditions, the Zr-based amorphous alloy exhibited worse wear resistance in phosphate buffer saline (PBS) and 0.9% NaCl solutions than that in air and deionized water, and the wear resistance is strongly influenced by the counterpart materials [18]. Moreover, because the pitting resistance is obviously influenced by the protein in the simulated body fluid, the wear resistance of Zr-based amorphous alloy is not as good as that of 316L SS, Ti6Al4V and CoCrMo although the wear resistance of Zr-based amorphous alloy is better in air and deionized water [19]. Meanwhile, comparing with the crystallized amorphous alloy, the amorphous alloy with amorphous structure exhibited lower wear resistance in all electrolytes including NaCl solution, phosphate buffer solution with or without protein [20]. Thus, as potentially applicable in the situations where corrosion and wear act simultaneously, more investigations on the tribocorrosion evaluations of amorphous alloys or amorphous coatings still need to be performed in the future. Especially, when the coating has variable chemical compositions resulted from dilution by laser melting, the tribocorrosion of amorphous alloy coatings contains more uncertainty than that of bulk amorphous alloys. Since

Fe-based coatings exhibited better amorphization than other amorphous alloy coatings, one Fe-based amorphous powder is selected for laser cladding in this work. Furthermore, because the chemical composition variations from the dilution effect will be suppressed gradually by multi-layer cladding, this work also aims to evaluate the effects of the number of deposition layers on the microstructure evolution and the tribocorrosion behavior. In light of the above, multi-layer Fe-based amorphous coatings were fabricated as tribocorrosion-resistant protective coatings using laser cladding. The microstructure evolution with different laser cladding layers and the corrosive wear behavior of the amorphous coatings in a simulated body fluid (Ringer's solution) were investigated.

2. Methodology

2.1 Materials

Fe-based amorphous powder (chemical compositions in wt.%: 4~9% Cr, 7~15% Mo, 2~5% Co, 3~6% Si, 3~6% Al, 2~5% Y and balance Fe) with a particle size of 45~75 μm was used for the alloy coating precursor. After mixing with a 4% PVA solution, the powder was pre-placed on the 316L SS substrate, and then dried in an oven at 100 °C. For comparing, one of the traditional bio-implant material AISI 316L austenitic stainless steel (SS) was also used in the present work with the following nominal chemical compositions (in wt.%): ≤0.08% C, 16.0~18.5% Cr, 10.0~14.0% Ni, 2.0~3.0% Mo, ≤2.0% Mn, ≤1.0% Si and balance Fe. GD-ECYW300 type pulse fiber laser was used for laser cladding with 3 kW peak power, 260 mm min^{-1} scanning speed and 12 Hz frequency. The thickness of the pre-placed amorphous powder for each layer is about 0.12 mm. After laser melting, the next amorphous powder layer was pre-placed on the former coating again, followed by laser melting. By repeating the procedure, a multi-layer coating was formed. Typical multi-layer Fe-based amorphous coatings with 1, 2, 4, 6, 9 and 12 layers were prepared using the same laser processing method and parameters.

2.2 Material characterization

X-ray diffraction (XRD) analysis was conducted on the alloy coatings to confirm the phase compositions. The XRD system (X'Pert HighScore Plus) was operated with Cu Ka radiation, and the diffraction angle (2θ) was varied from 20° to 80°. A HXD-1000TC digital microhardness tester was used for the hardness tests and an average value was obtained from 5 randomly located positions on the cross-sectional coating for each sample. The indentations were made under a constant load of 1.96 N within 15 s. The microstructure morphologies were observed for Fe-based alloy coatings under a scanning electron microscope (SEM). The worn surface morphologies of the tested specimen and the counterface were examined by optical and SEM for the analysis of corrosive wear mechanisms.

2.3 *Tribocorrosion Testing*

Specimens for tribocorrosion tests were cut to dimensions of 1 cm×2 cm×1 cm and then polished with 1,000-grit SiC paper to obtain an average surface roughness (R_a) of 0.1 μm. Before the tribo-corrosion tests, the specimens were covered by insulating lacquer except for an area of 1×2 cm^2 which would be exposed to the solution during tribocorrosion testing.

The tribocorrosion test was performed on a laboratory scale reciprocating wear test machine, which has been described in detail elsewhere [21]. A contact load of 10 N was used for all tests at a frequency of 1 Hz with an amplitude of 8 mm. The total duration time was 60 min and all the tests were performed at 37.5 °C. An Alumina ball with an 8 mm diameter was held stationary as a counterpart during sliding. The test cell, the ball holder and all other fixtures were made of nylon. Electrochemical measurements were performed by an ACM GILL AC potentiostat and the potentiostat can record or control the potential and the current during sliding. The test specimen was served as a working electrode, a platinum wire was used as the auxiliary electrode, and a saturated calomel electrode (SCE) was served as the reference electrode. All the electrochemical potentials are reported vs SCE. During

sliding at open circuit, the OCP was continuously recorded together with the coefficient of friction as a function of time. In addition, tribocorrosion tests were also conducted under potentiostatic conditions, and the current was measured at constantly applied potentials 100 mV_{SCE} and -600 mV_{SCE}. After each test, using a stylus surface profilometer, the surface profiles across each wear track at four locations were measured for the evaluation of the total wear volume by multiplying the average cross-sectional area and the wear-track length. Furthermore, to analysis the dynamic corrosion resistance, the anodic polarization curves were also measured for some of the specimens with and without sliding at a sweep rate of 1 mV s^{-1}, starting from −550 mV (vs. SCE) and ending at 700 mV (vs. SCE) or when the current density reached 10 mA cm^{-2}. However, the friction coefficient and the wear volume loss were abandoned when applying these polarization curve measurements.

3. Results

3.1 Microstructure and hardness

Figure 1 shows the XRD patterns of laser clad coatings with different layers. Only the peaks of γ-Fe can be seen from the XRD pattern of 1-layer coating, indicating the chemical composition is close to the substrate 316L SS. The peaks of γ-Fe and α-Fe present in the XRD pattern of 2-layer coating, suggesting this coating is composed of γ-Fe and α-Fe solid solutions. Because of dilution, the reflection intensities of the γ-Fe peaks from the 316L stainless steel substrate diminish with increasing the cladding layer. When the cladding layer increases to 4 and 6 layers, there are only α-Fe peaks exhibited in their XRD patterns. And the diffuse peak near 42 degree indicates the presence of an amorphous phase. On the XRD patterns of 9 and 12 layers, the α-Fe peak is suppressed and presents with some unknown peaks. The small multiple peaks may come from the crystallization of the amorphous phase. Because of dilution, multi-layer laser cladding favors to obtain a similar chemical composition with the

original amorphous powder and then form the amorphous phase in the coating. Therefore, with the increasing cladding layer, the microstructure evolves from γ-Fe to α-Fe solid solution, and then to a mixture with crystalline and amorphous phases.

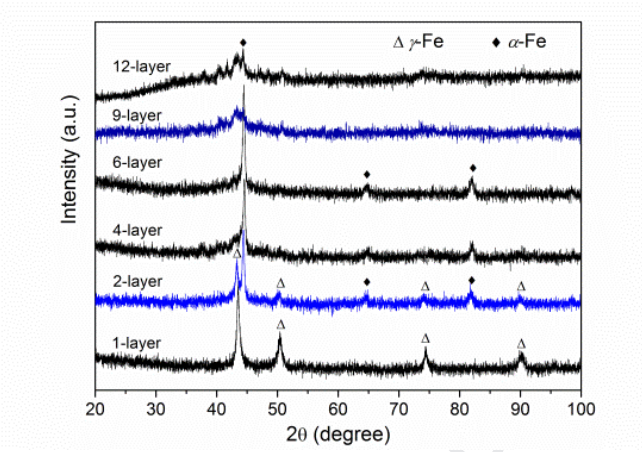

Fig. 1. XRD patterns of the laser clad coatings.

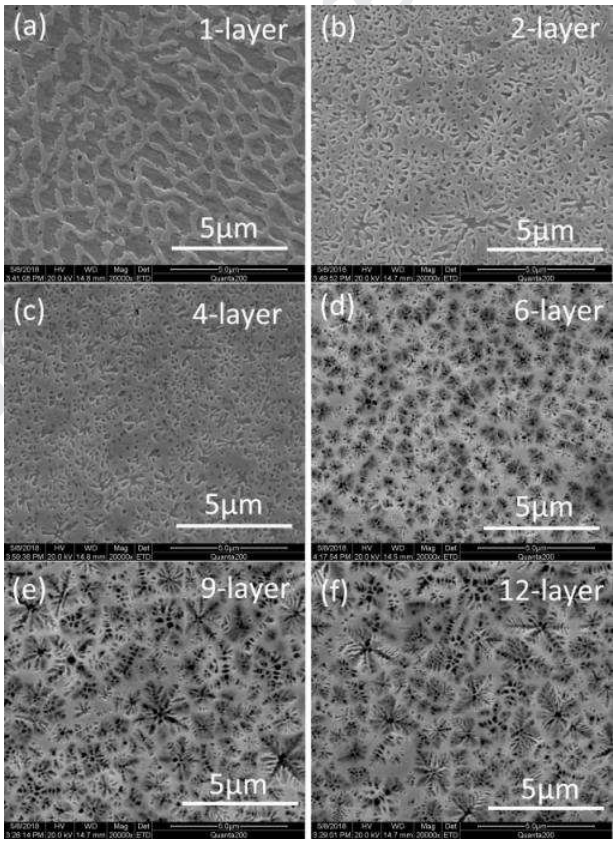

Fig. 2. SEM images for the microstructure of coatings with different cladding layer.

Direct observation on the microstructure of laser clad coatings was done by SEM, as shown in Fig. 2. The grey network structure and the dark background can be seen in the 1-layer coating. The amount

of the grey network in the 2-layer coating increases obviously, indicating that this is an α-Fe solid solution and the dark area is a γ-Fe solid solution, as shown in Fig. 1. In the 4-layer coating, the grey area increases continually, and the dark area decreases so much that it can't be determined by XRD. The SEM morphology of 6-layer coating consists of white area and small dendrites (around 1 μm in size), indicating that the white area is the amorphous phase based on the XRD pattern. The amorphous phase has been confirmed by Focused Ion Beam (FIB) combined with TEM (Transmission Electron Microscopy) in our further work. Both of the XRD patterns and the morphologies of the 9-layer and 12-layer coatings are similar, and they compose of amorphous phase and dendrites. So the typical amorphous composite coating is formed by an amorphous phase and some dendrites embedded in the amorphous matrix.

Because of the importance of the chemical composition, EDS analysis with surface scanning was performed on all of the coatings, as shown in Fig. 3. As can be seen, the alloying elements from the amorphous powder increase with the number of the cladding layers. Moreover, comparing with the dark area, the white area contains more Mo, Y, Si, Cr, Co, but less Al, Fe, Ni in the same coating as shown in Fig. 2. So the chemical composition of the laser clad coating varies with the number of the laser cladding layer.

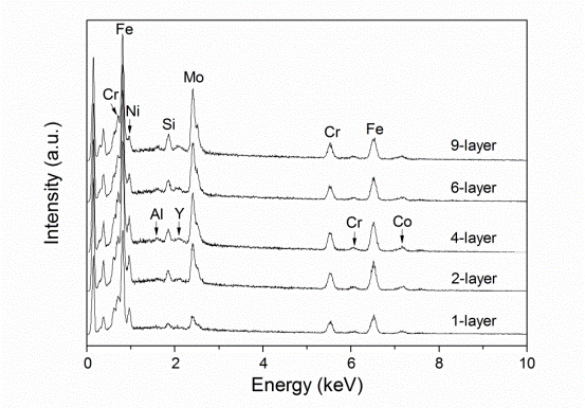

Fig. 3. EDS analysis on the top surface of laser clad coating before sliding wear.

With the increase of the cladding layers, the microstructure evolution influences the coating hardness, as shown in Fig. 4. The hardness of the coating cross-section shows that the hardness improves about 3 times from 1 to 12 cladding layers, and the 12-layer coating obtained the highest hardness, which is more than 1200 HV. However, on the coating cross-section, the hardness decreases gradually with the depth. Except for the change of chemical composition resulted from dilution, the amorphous phase crystallization and the crystal phase coarsening due to the repeated heating caused by melting of the upper layer may be also responsible for the decreasing hardness on the cross-section.

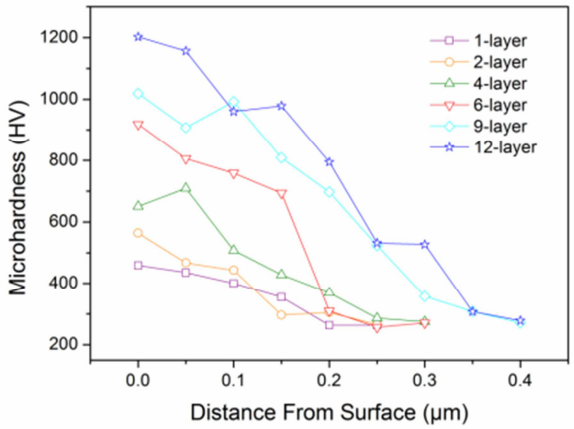

Fig. 4. Microhardness tests for the cross-section of the laser clad coatings.

3.2 Polarization behavior

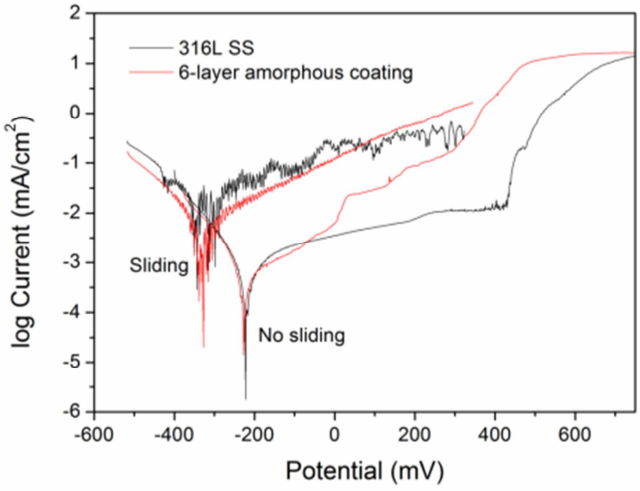

Fig. 5. Anode polarization curves measured for the test samples in Ringer's solution at a scan rate of 1 mV s^{-1}.

The potentiodynamic polarization behaviour of 316L SS and 6-layer coating in Ringer's solution was measured with and without sliding at a scan rate of 1 mV s^{-1}. Fig. 5 shows the obtained anodic polarization curves, which reveal that sliding causes the reduction of the corrosion potential and the increase of the passivity current density. The significant passivation can be seen in the anode region of 316 SS. Due to the damage or even removal of the passive film [22], an increase in the passivity current density of 316L SS was more significant during sliding. Moreover, the passivity current density of 6-layer coating is a little lower than that of 316L SS during sliding although their passivity current densities are similar when no sliding.

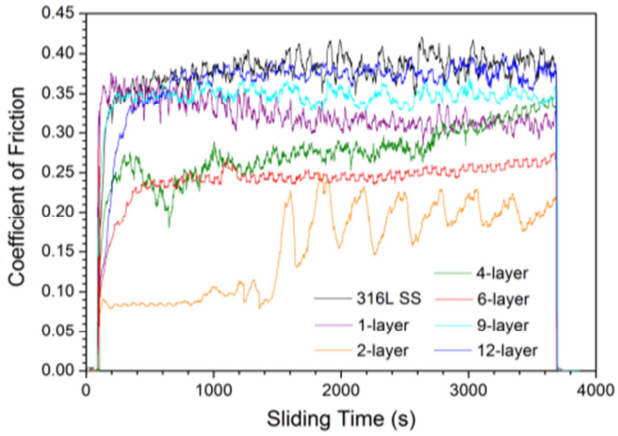

Fig. 6. Coefficient of friction recorded for 316L SS and laser clad coatings during sliding in Ringer's solution at open circuit.

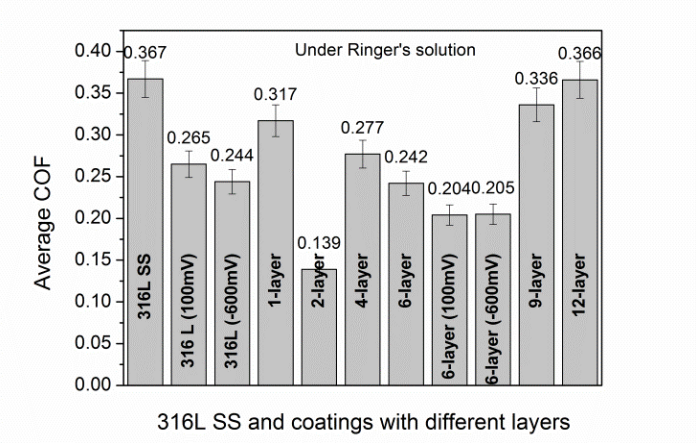

Fig. 7. Average values of the Coefficient of friction calculated for 316L SS and laser clad coatings sliding in Ringer's solution at open circuit.

3.3 Tribocorrosion test

To analyze the influence of the number of cladding layers on friction and wear, tribocorrosion tests without externally applied potentials (OCP) were performed. Figure 6 shows the coefficient of friction (COF) for the Fe-based alloy coatings and 316L SS in Ringer's solution. The corresponding average COF is shown in Fig. 7. With increasing cladding layers, the COF decreases firstly and then increases. Except for the 12-layer coating, the COF values of laser clad coatings are lower than that of 316L SS. Interestingly, the 2-layer coating possesses the lowest COF (0.139) among all specimens, which is much lower than 316L SS (0.367) and 12-layer coating (0.366). This could be due to the 2-layer coating structure which comprises a mixture of α and γ solid solution. Further work is required to clarify this phenomenon.

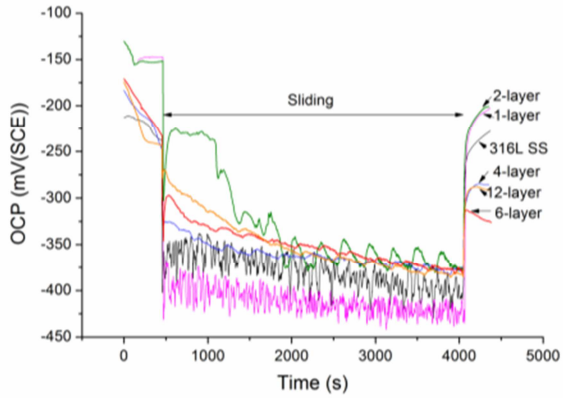

Fig. 8. Open circuit potential detected for 316L SS and amorphous composite coatings during sliding in Ringer's solution.

During each tribocorrosion test in Ringer's solution, the open circuit potential (OCP) was recorded for all specimens, as shown in Fig. 8. Similar OCP evolution behaviour can be seen for the 4-layer, 6-layer, and 12-layer specimens as shown in Fig. 8: after the initial sudden drop at the beginning of the sliding, the OCP then decreased slowly and smoothly with sliding time. Comparing with 316L SS, the 1-layer coating exhibits a lower OCP. Due to the low surface hardness, sliding of the 1-layer coating caused a wider wear track, which leads to a drop in OCP. However, except for the 1-layer coating, OCP

during sliding for other coatings was higher than that for the 316 SS.

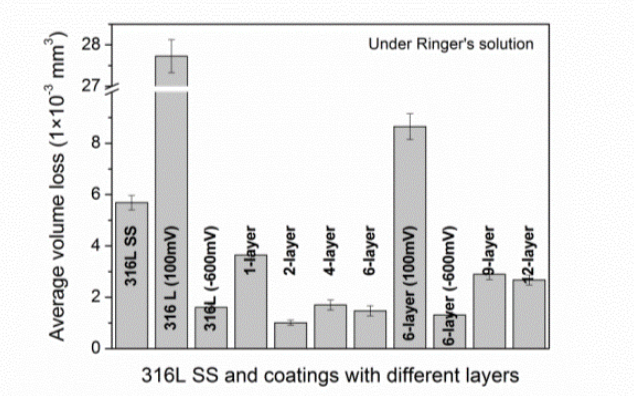

Fig. 9. Volume loss calculated from the wear tracks of 316L SS and laser clad coatings after sliding wear in Ringer's solution.

The effect of the number of cladding layers on the volume loss of amorphous composite coatings in Ringer's solution is illustrated in Fig. 9. Generally, the volume loss decreases firstly and then increases with the increasing cladding layers, which is similar to the trend of COF. The volume loss of 316L SS is 5.7×10^{-3} mm^3, which is about 5.6 times higher than that of 2-layer coating and more than 2 times higher than that of 12-layer coating. Therefore, the laser clad composite coatings in Ringer's solution exhibit a better tribocorrosion property at OCP. Especially, the 2-layer coating possesses the lowest COF and the best wear resistance. Furthermore, the amorphous powder formed coatings with 1, 2, and 3 layers are being investigated in our next step.

To analyze the influence of electrochemical potentials on friction and wear, tribocorrosion tests at cathodic and anodic potentials were conducted. Fig. 10 shows the relationship between the current transients and the time recorded for 316L SS and 6-layer coating before, during and after sliding in Ringer's solution under a potentiostatic condition at a potential of 100 mV_{SCE} and -600 mV_{SCE}, respectively. At the anodic potential of 100 mV_{SCE}, for both specimens, the current during sliding increased obviously, suggesting wear-induced corrosion. At 100 mV_{SCE}, the current of 316L SS during sliding fluctuated around 0.3 mA, while that of 6-layer coating gradually increased with the duration

time. In the 316L SS, the relative constant current during sliding is a consequence of the cyclic depassivation and repassivation mechanism. The current recorded for 316L SS during sliding fluctuated could be attributed to a competition between mechanical depassivation and electrochemical passivation rates [23]. The different current transient behavior of the 6-layer coating could be due to the generation of some micro cracks during laser cladding and during sliding, which resulted in the increased current during sliding and prevented repassivation after sliding, because more sub-surface and even substrate could be exposed to the solution. At a cathodic potential of -600 mV_{SCE}, the cathodic current of 6-layer coating during sliding was obviously lower than that of 316L SS, in consistency with the potentiodynamic testing results shown in Fig. 10(b).

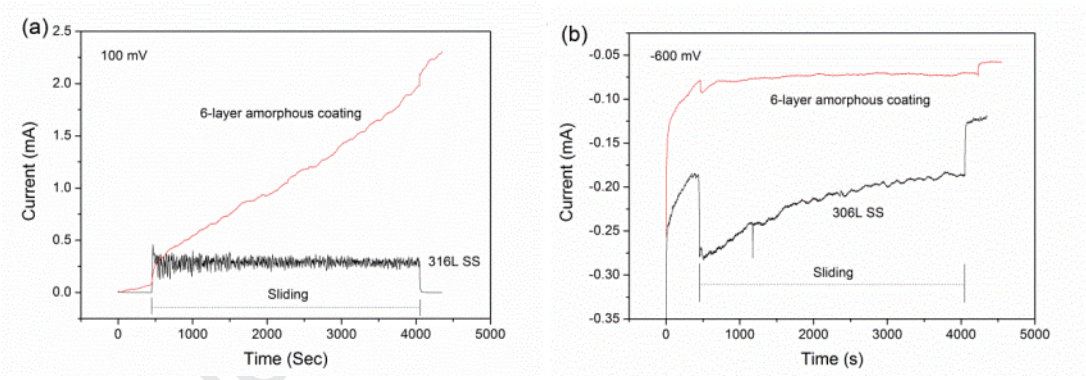

Fig. 10. Current transients recorded for 316L SS and 6-layer coating before, during and after sliding in Ringer's solution under potentiostatic condition at an anodic potential of (a) 100 mV_{SCE} and (b) -600 mV_{SCE}.

Correspondingly, the average COF and the average volume loss of 316L SS and 6-layer coating sliding in Ringer's solution under potentiostatic conditions at a potential of 100 mV_{SCE} and -600 mV_{SCE} are shown in Fig. 7 and Fig. 9, respectively. The fixed potential of 100 mV_{SCE} or -600 mV_{SCE} favors reducing the COF for both specimens, especially for 316L SS. On the other side, a significant increase in the volume losses for both 316L SS and the 6-layer coating at an anodic potential of 100 mV_{SCE} can be seen in Fig. 9.

3.4 Worn surface morphology

The surface micrographs of 316L SS and laser clad coatings tested in Ringer's solution at OCP are shown in Fig. 11. All the wear tracks are characterized by many plowing marks, suggesting abrasive wear is the primary wear mechanism at OCP. 316L SS exhibits the roughest surface, which corresponds to the biggest volume loss, as shown in Fig. 8. The surface of the wear track of the 2-layer coating is very smooth, which is consistent with the minimum amount of wear, as shown in Fig. 8. Meanwhile, as shown in Fig. 11(c), some pit-like features presents in the center of the wear track where the highest contact stress is, indicating a fatigue wear mechanism for the 2-layer coating. Although the 9-layer and 12-layer coatings have higher hardness, their wear tracks didn't show smooth grooves with fine scratching marks, indicating the high hardness does not always favor to improve the wear resistance. Moreover, the coating with high hardness may promote the wear on the surface of Alumina ball, which in turn accelerates the wear of the coating itself due to the roughened surface of the counterpart.

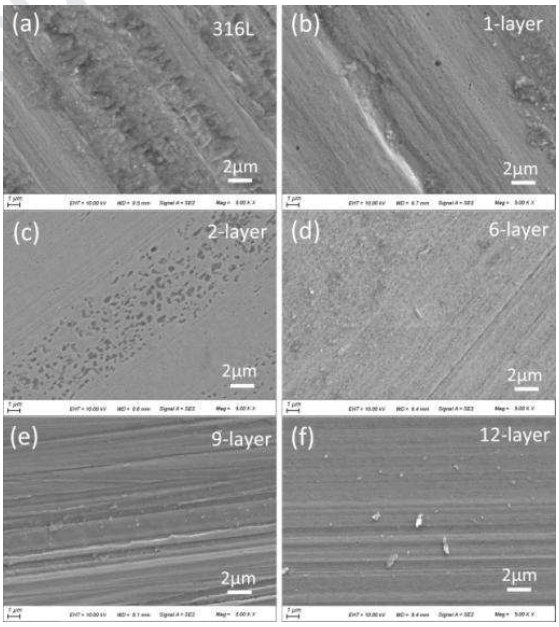

Fig. 11. Worn surface morphologies of 316L SS and laser clad coatings after tribocorrosion test in Ringer's solution at OCP, (a) 316L SS; (b) 1-layer coating; (c) 2-layer coating; (d) 6-layer coating; (e)

9-layer coating; (f) 12-layer coating.

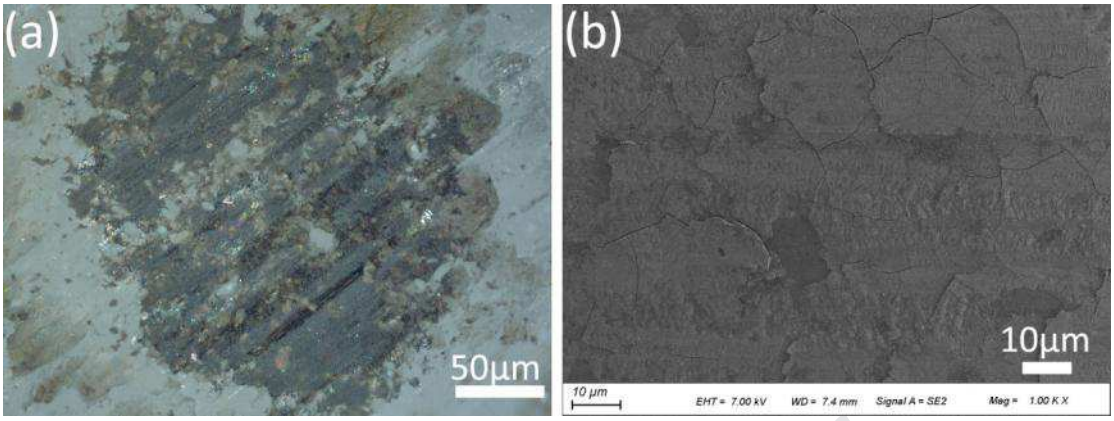

Fig. 12. Surface morphology observation for the ball after sliding against 9-layer coating in Ringer's solution at OCP by (a) optical microscope and (b) SEM.

The surface morphology of the Alumina ball was observed after sliding against the 9-layer coating in Ringer's solution at OCP, as shown in Fig. 12. As can be seen, the ball surface presents a thick tribo-layer composed of debris covered on some grooves. It indicates that not only the hard alumina slider but also the transferred material on the slider surface lead to the abrasive wear [24]. Since the tribo-layer formed from the corrosion products and wear debris, it may work as a lubricant which leads to the decrease of COF. The tribocorrosion behavior of the laser clad coating is also strongly influenced by the material transfer during the tribocorrosion process.

4. Discussion

4.1 Volume loss of corrosive wear

As mention in the previous literature [18-20], the amorphous alloy does not possess good corrosive wear resistance in some cases. With the increasing number of deposition layers, the content of the amorphous phase increases in the Fe-based alloy coating, as shown in Fig. 1 and 2. However, since the amorphous phase and the crystallized phase are brittle, the increase of amorphous content increases the brittleness of coating, which deteriorates the sliding wear resistance, evidenced by the worn surfaces shown in Fig. 11(e) and (f). In addition, the brittle coating also favors generating thermal

and fatigue cracks, which results in crevice corrosion. On the other hand, the crystalline structure of the amorphous alloy could show better corrosive wear resistance than the BMG material with amorphous structure due to a nanocrystallization process [20]. Further, since the abrasion of the passive film induces wear accelerated corrosion and the presence of the passive film significantly increases subsurface deformation [25], the passive film formed in the corrosive solution plays a key role in the material removal. Meanwhile, the galvanic coupling could be established between the depassivated wear track and the surrounding passive area [26]. For the amorphous composite coating, because the corrosion resistance does not mainly depend on the passivation, the effects of the passive film and the galvanic corrosion are less than those on 316L SS. Therefore, except for the lowest hardness, the significant passivation (as shown in Fig. 5) is responsible for the largest volume loss of 316 SS.

4.2 *Effect of electrochemical potential*

The electrochemical conditions determine material deterioration and the electrochemical potentials strongly influence the tribological behavior. Under an electrochemical potential, an electric double layer can be generated which consists of a compact layer (ions are strongly attracted to the wall surface and are immobile) and a diffuse double layer (ions are affected less by the electrical field and are mobile) [27]. For the effect of hydrodynamic lubrication, the COF is varied with the electrochemical potentials. So the COFs decreased obviously after applying the potentials of -600 mV_{SCE} and 100 mV_{SCE} in this case. Meanwhile, the volume loss is also strongly influenced by the electrochemical potentials. Because more strain is accumulated below the surface at passivly applied potentials [28], the volume loss is higher at an anodic potential than in a cathodic potential, especially for the condition of high applied load and speed [29]. Similar observations have been made by other investigators. For example, friction and wear of SiC were decreased under cathodic electrochemical

polarization [27]. Even a threshold electrode potential could be found for a transition from low to high wear coefficients [30]. The present study shows that the volume loss of 316L SS and the 6-layer coating at 100 mV_{SCE} increased respectively about 5 and 6 times more than those at OCP. It increased dramatically at high potentials where passivity triggered severe wear accelerated corrosion and promoted mechanical wear [31]. Therefore, the volume losses are much lower at -600 mV_{SCE} than those at 100 mV_{SCE} for both materials of 316L SS and 6-layer coating.

4.3 Mechanical wear and chemical wear

There have been several attempts at the quantification of tribocorrosion to determine the contributions of mechanical wear, corrosion and their synergism to the total material loss. One of the approach is the synergistic approach, which is described as $W_{total} = W_{corr} + W_{wear} + \Delta W$, where W_{total} is the total material loss, W_{wear} is the pure mechanical wear loss, W_{corr} is the material loss due to corrosion only and ΔW is the material loss increment due to the synergy between corrosion and wear [32, 33]. Pure mechanical wear W_{wear} means the material loss only due to mechanical contact, excluding any material loss related to corrosion. The pure corrosion component W_{corr} can be ignored for passive metals at OCP and in the passivation potential region because of the low currents produced. Thus, if the pure mechanical wear (W_{wear}) in the solution could be measured, then ΔW would be determined by the difference between W_{total} and W_{wear}. A technique has been suggested and used by several investigators [29, 34, 35] to evaluate the pure mechanical wear in the test solution, which involved wear testing at a cathodic potential. Since corrosion is limited by cathodic protection (although it does not mean there is absolutely no corrosion), the material loss measured under cathodic potentials in the same media was generally adopted as pure mechanical wear loss W_{wear}. If so, then the volume losses of 316L SS and the 6-layer coating measured at -600 mV_{SCE} in Ranger's solution could be regarded as pure mechanical

wear loss W_{wear}. As shown in Fig. 9, the volume losses of 316L SS and 6-layer coating at -600 mV_{SCE} are 1.60 $\times 10^{-3}$ mm^3 and 1.31 $\times 10^{-3}$ mm^3, while those values at OCP are 5.68 $\times 10^{-3}$ mm^3 and 1.47 $\times 10^{-3}$ mm^3, respectively. The percentage of pure mechanical wear equals W_{wear} / W_{total}. So the percentage of pure mechanical wear of 316L SS at OCP is 28.2%, while the corresponding rate for 6-layer coating is 89.1%. It suggests that at OCP the predominant tribocorrosion mechanism of the 6-layer coating is mechanical wear in comparison with 316L SS.

Although the synergistic approach provides the possibility of quantifying tribocorrosion, it gives little indication of the underlying mechanisms involved. There are also uncertainties in the determination of the pure mechanical wear component, W_{wear}, by arbitrarily using a cathodic potential. The cathodic reactions, such as proton reduction and hydrogen evolution, which are strongly affected by the value of the applied cathodic potential, may lead to hydrogen gas formation at the contact interface and hydrogen segregation at the surface, leading to the modification of the contact condition and material surface properties. It is highly likely that the W_{wear} value measured is potential dependent. To overcome these uncertainties, a mechanistic approach has been used in many recent publications [36-40]. In this approach, material loss is combined with sliding and corrosion conditions as a result of two mechanisms: mechanical wear (V_{mech}) and chemical wear (V_{chem}). The former is due to mechanical contact which produces metallic wear particles and exposes fresh metal, while the latter includes material losses associated with the anodic currents, i.e. metal dissolution from the freshly exposed metal surface and wearing or removal of the oxide film formed at sliding contact intervals. Accordingly, the total material loss, V_{total}, can be expressed as follows:

$$V_{total} = V_{mech} + V_{chem} \quad (1)$$

The chemical wear component (V_{chem}) can be estimated by the excess current measured during sliding

according to the Faraday's law:

$$V_{chem} = \frac{I_r t M}{nF\rho} \quad (2)$$

where t is the sliding time, I_r is the excess current flowing through the sliding track, F is the Faraday's constant, ρ is the density of the material and M is the atomic mass of the alloy. The valance of corrosion, n, is assumed to be 3 to account for chromium oxide formation on both 316L SS and the coating, both containing chromium as the major passive film formation element. At OCP, the corrosion currents during sliding are determined by the polarization curves shown in Fig. 5, using the Tafel method. At 100 mV_{SCE}, the measured currents during sliding are used directly for the calculation. In both cases, the contribution of the area outside the sliding track is ignored.

Table 1 summarizes the various components of material loss at OCP. It can be seen that at OCP, the 6-layer coating reduces both the chemical wear and mechanical wear, and thus total material loss, as compared to those of 316LSS. Mechanical wear contributes to 76% and 61% of the total material loss from 316L SS and the 6-layer coating, respectively, suggesting that the higher hardness of the 6-layer coating is beneficial in reducing the contribution of mechanical wear. At 100 mV_{SCE}, the V_{chem} component can be calculated from the measured current transient curve shown in Fig. 10(a) for 316L SS. The V_{chem} value calculated is 19.2 $\times 10^{-3}$ mm^3, and the V_{total} measured is 27.7 $\times 10^{-3}$ mm^3 (Fig. 9). Thus, at 100 mV_{SCE}, mechanical wear of 316L SS is 8.5 $\times 10^{-3}$ mm^3, which contributes to 31% of total material loss. The dominance of chemical wear (69%) at 100 mV_{SCE} is obviously due to the increased anodic dissolution and oxide film growth kinetics. It is also noted that the V_{chem} and V_{mech} values of 316L SS at 100 mV_{SCE} are much larger than those at OCP, suggesting much enhanced wear accelerated corrosion and corrosion accelerated mechanical wear at the anodic potential. However, for the 6-layer coating at 100 mV_{SCE}, the current increases continuously due to localized corrosion through the

existing micro cracks (Fig.10a), and thus it is impractical to evaluate the V_{chem} component from the measured current arising from localized corrosion.

Table 1 Summary of measured V_{total}, calculated V_{chem} and derived V_{mech} at OCP for the 316L SS and the 6-layer alloy coating.

	V_{total} (mm^3)	V_{chem} (mm^3)	V_{mech} (mm^3)	% mechanical wear
316L SS	$5.68x10^{-3}$	$1.36x10^{-3}$	$4.32x10^{-3}$	76
6-layer	$1.47x10^{-3}$	$5.72x10^{-4}$	$8.98x10^{-4}$	61

5. Conclusions

(1) A series of Fe-based alloy coatings was deposited on 316L SS by laser cladding with Fe-based amorphous powder. With the increasing number of cladding layers, the chemical composition changes, the surface hardness increases gradually to over 1200 HV, and the microstructure evolves from γ-Fe to α-Fe solid solution, and then to a mixture with dendritic crystal and amorphous phases.

(2) The sliding wear in Ringer's solution at OCP shows the COF and the volume loss decrease firstly and then increase when the cladding layer increases. The 2-layer coating exhibits the lowest COF and the lowest wear loss, which are about 3 and 5.6 times lower than that of 316L SS.

(3) The role of cathodic protection at -600 mV_{SCE} for 316L SS is more significant than that for the 6-layer coating. The predominant tribocorrosion mechanism of 6-layer coating at OCP is mechanical wear in comparison with 316L SS. The lowest hardness and the passivation characteristic contributes to the largest volume loss of 316 SS.

(4) At an applied anodic potential of 100 mV_{SCE}, chemical wear becomes more dominant for 316LSS, and localized corrosion occurs in the 6-layer coating through the pre-existing micro

cracks.

Author information

Corresponding Author

*Tel.: +86 519 85191969. E-mail: xiulinji@gmail.com (X.J.); ysun01@dmu.ac.uk (Y.S.).

Notes

The authors declare no competing financial interest.

Acknowledgments

This research was supported by the National Natural Science Foundation of China (51875169, 51505126, and 51475140). The authors also acknowledge the support from the Royal Society-NSFC International Exchange Program (IE161010, 51711530226).

References

[1] J. Dufils, M.A. Wimmer, J. Kunze, M.T. Mathew, M.P. Laurent, Influence of molybdate ion and pH on the fretting corrosion of a CoCrMo – Titanium alloy couple, Biotribology, 11 (2017) 20-28.
[2] B. Sivakumar, L.C. Pathak, R. Singh, Fretting corrosion response of boride coated titanium in Ringer's solution for bio-implant use: Elucidation of degradation mechanism, Tribology International, 127 (2018) 219-230.
[3] C. Hee Ay, C. Dipankar, N. Md Julker, O. Noor Azuan Abu, Effects of surface coating on reducing friction and wear of orthopaedic implants, Science and Technology of Advanced Materials, 15 (2014) 014402.
[4] D. Zenebe, S. Yi, S.S. Kim, Sliding friction and wear behavior of Fe-based bulk metallic glass in 3.5% NaCl solution, Journal Of Materials Science, 47 (2012) 1446-1451.
[5] J. Chen, W. Cai, Effect of scratching frequency on the tribocorrosion resistance of Al-Mn amorphous thin films, Wear, 426-427 (2019) 1457-1465.
[6] J.J. Lai, Y.S. Lin, C.H. Chang, T.Y. Wei, J.C. Huang, Z.X. Liao, C.H. Lin, C.H. Chen, Promising Ta-Ti-Zr-Si metallic glass coating without cytotoxic elements for bio-implant applications, Applied Surface Science, 427 (2018) 485-495.
[7] B. Zhang, J. Cheng, X. Liang, Effects of Cr and Mo additions on formation and mechanical properties of Arc-sprayed FeBSiNb-based glassy coatings, Journal of Non-Crystalline Solids, 499 (2018) 245-251.
[8] C. Jiang, W. Liu, G. Wang, Y. Chen, Y. Xing, C. Zhang, M. Dargusch, The corrosion behaviours of plasma-sprayed Fe-based amorphous coatings, Surface Engineering, 34 (2018) 634-639.
[9] H.R. Ma, J.W. Li, J. Jiao, C.T. Chang, G. Wang, J. Shen, X.M. Wang, R.W. Li, Wear resistance of Fe-based amorphous coatings prepared by AC-HVAF and HVOF, Materials Science and Technology, 33 (2017) 65-71.
[10] F.Y. Shu, S. Liu, H.Y. Zhao, W.X. He, S.H. Sui, J. Zhang, P. He, B.S. Xu, Structure and high-temperature property of amorphous composite coating synthesized by laser cladding FeCrCoNiSiB high-entropy alloy powder, Journal Of Alloys And Compounds, 731 (2018) 662-666.
[11] P.L. Zhang, H. Yan, C.W. Yao, Z.G. Li, Z.S. Yu, P.Q. Xu, Synthesis of Fe-Ni-B-Si-Nb amorphous and

crystalline composite coatings by laser cladding and remelting, Surface & Coatings Technology, 206 (2011) 1229-1236.

[12] A. Basu, A.N. Samant, S.P. Harimkar, J.D. Majumdar, I. Manna, N.B. Dahotre, Laser surface coating of Fe–Cr–Mo–Y–B–C bulk metallic glass composition on AISI 4140 steel, Surface and Coatings Technology, 202 (2008) 2623-2631.

[13] D.T.A. Matthews, V. Ocelík, D. Branagan, J.T.M. de Hosson, Laser engineered surfaces from glass forming alloy powder precursors: Microstructure and wear, Surface and Coatings Technology, 203 (2009) 1833-1843.

[14] X.L. Wu, Y.S. Hong, Fe-based thick amorphous-alloy coating by laser cladding, Surface & Coatings Technology, 141 (2001) 141-144.

[15] M. Yasir, C. Zhang, W. Wang, Z.W. Zhang, L. Liu, Tribocorrosion Behavior of Fe-Based Amorphous Composite Coating Reinforced by Al2O3 in 3.5% NaCl Solution, Journal Of Thermal Spray Technology, 25 (2016) 1554-1560.

[16] X.L. Ji, B.A. Hu, Y.X. Li, S.Q. Wang, Sliding tribocorrosion behavior of bulk metallic glass against bearing steel in 3.5% NaCl solution, Tribology International, 91 (2015) 214-220.

[17] Q. Chen, K.C. Chan, L. Liu, Tribological characterisation of Zr-based bulk metallic glass in simulated physiological media, Philosophical Magazine, 91 (2011) 3705-3715.

[18] N.B. Hua, W.Z. Chen, W.G. Wang, H.T. Lu, X.Y. Ye, G.H. Li, C. Lin, X.F. Huang, Tribological behavior of a Ni-free Zr-based bulk metallic glass with potential for biomedical applications, Materials Science & Engineering C-Materials for Biological Applications, 66 (2016) 268-277.

[19] Y. Wang, L.L. Shi, D.L. Duan, S. Li, J. Xu, Tribological properties of Zr61Ti2Cu25Al12 bulk metallic glass under simulated physiological conditions, Materials Science & Engineering C-Materials for Biological Applications, 37 (2014) 292-304.

[20] N. Espallargas, R.E. Aune, C. Torres, N. Papageorgiou, A.I. Munoz, Bulk metallic glasses (BMG) for biomedical applications-A tribocorrosion investigation of Zr55Cu30Ni5Al10 in simulated body fluid, Wear, 301 (2013) 271-279.

[21] Y. Sun, Tribocorrosive behaviour of low temperature plasma-nitrided PH stainless steel sliding against alumina under linear reciprocation with and without transverse oscillations, Wear, 362 (2016) 105-113.

[22] H.-H. Ge, G.-D. Zhou, W.-Q. Wu, Passivation model of 316 stainless steel in simulated cooling water and the effect of sulfide on the passive film, Applied Surface Science, 211 (2003) 321-334.

[23] P. Ponthiaux, F. Wenger, D. Drees, J.P. Celis, Electrochemical techniques for studying tribocorrosion processes, Wear, 256 (2004) 459-468.

[24] Y. Sun, R. Bailey, Improvement in tribocorrosion behavior of 304 stainless steel by surface mechanical attrition treatment, Surface & Coatings Technology, 253 (2014) 284-291.

[25] S. Guadalupe Maldonado, S. Mischler, M. Cantoni, W.-J. Chitty, C. Falcand, D. Hertz, Mechanical and chemical mechanisms in the tribocorrosion of a Stellite type alloy, Wear, 308 (2013) 213-221.

[26] G.H. Zhao, R.E. Aune, H.H. Mao, N. Espallargas, Degradation of Zr-based bulk metallic glasses used in load-bearing implants: A tribocorrosion appraisal, Journal Of the Mechanical Behavior Of Biomedical Materials, 60 (2016) 56-67.

[27] T. Amann, A. Kailer, M. Herrmann, Influence of Electrochemical Potentials on the Tribological Behavior of Silicon Carbide and Diamond-Coated Silicon Carbide, Journal of Bio- and Tribo-Corrosion, 1 (2015) 30.

[28] J. Perret, E. Boehm-Courjault, M. Cantoni, S. Mischler, A. Beaudouin, W. Chitty, J.P. Vernot, EBSD,

SEM and FIB characterisation of subsurface deformation during tribocorrosion of stainless steel in sulphuric acid, Wear, 269 (2010) 383-393.

[29] D.F. Ferreira, S.M.A. Almeida, R.B. Soares, L. Juliani, A.Q. Bracarense, V.d.F.C. Lins, R.M.R. Junqueira, Synergism between mechanical wear and corrosion on tribocorrosion of a titanium alloy in a Ringer solution, Journal of Materials Research and Technology, 8 (2019) 1593-1600.

[30] S. Mischler, A.I. Muñoz, Wear of CoCrMo alloys used in metal-on-metal hip joints: A tribocorrosion appraisal, Wear, 297 (2013) 1081-1094.

[31] A. Bazzoni, S. Mischler, N. Espallargas, Tribocorrosion of Pulsed Plasma-Nitrided CoCrMo Implant Alloy, Tribology Letters, 49 (2013) 157-167.

[32] S.W. Watson, F.J. Friedersdorf, B.W. Madsen, S.D. Cramer, Methods of measuring wear-corrosion synergism, Wear, 181-183 (1995) 476-484.

[33] Y. Huang, X. Jiang, S. Li, Pure mechanical wear loss measurement in corrosive wear, Bulletin of Materials Science, 23 (2000) 539-542.

[34] W.J. Tomlinson, I.D. Molyneux, Corrosion, erosion-corrosion, and the flexural strength of WC-Co hardmetals, Journal of Materials Science, 26 (1991) 1605-1608.

[35] W.J. Tomlinson, M.G. Talks, Erosion and corrosion of cast iron under cavitation conditions, Tribology International, 24 (1991) 67-75.

[36] S. Mischler, Triboelectrochemical techniques and interpretation methods in tribocorrosion: A comparative evaluation, Tribology International, 41 (2008) 573-583.

[37] D. Landolt, S. Mischler, M. Stemp, Electrochemical methods in tribocorrosion: a critical appraisal, Electrochimica Acta, 46 (2001) 3913-3929.

[38] Y. Sun, E. Haruman, Tribocorrosion behaviour of low temperature plasma carburised 316L stainless steel in 0.5 M NaCl solution, Corrosion Science, 53 (2011) 4131-4140.

[39] S. Barril, S. Mischler, D. Landolt, Triboelectrochemical investigation of the friction and wear behaviour of TiN coatings in a neutral solution, Tribology International, 34 (2001) 599-608.

[40] S. Mischler, A. Spiegel, M. Stemp, D. Landolt, Influence of passivity on the tribocorrosion of carbon steel in aqueous solutions, Wear, 251 (2001) 1295-1307.

Figure captions

Fig. 1. XRD patterns of the laser clad coatings.

Fig. 2. SEM images for the microstructure of coatings with different cladding layer.

Fig. 3. EDS analysis on the top surface of laser clad coating before sliding wear.

Fig. 4. Microhardness tests for the cross-section of the laser clad coatings.

Fig. 5. Anode polarization curves measured for the test samples in Ringer's solution at a scan rate of 1 mV s^{-1}.

Fig. 6. Coefficient of friction recorded for 316L SS and laser clad coatings during sliding in Ringer's solution.

Fig. 7. Average values of the Coefficient of friction calculated for 316L SS and laser clad coatings sliding in Ringer's solution.

Fig. 8. Open circuit potential detected for 316L SS and amorphous composite coatings during sliding in Ringer's solution.

Fig. 9. Volume loss calculated from the wear tracks of 316L SS and laser clad coatings after sliding wear in Ringer's solution.

Fig. 10. Current transients recorded for 316L SS and 6-layer coating before, during and after sliding in Ringer's solution under potentiostatic condition at an anodic potential of (a) 100 mV_{SCE} and (b) -600 mV_{SCE}.

Fig. 11. Worn surface morphologies of 316L SS and laser clad coatings after tribocorrosion test in Ringer's solution, (a) 316L SS; (b) 1-layer coating; (c) 2-layer coating; (d) 6-layer coating; (e) 9-layer coating; (f) 12-layer coating.

Fig. 12. Surface morphology observation for the ball after sliding against 9-layer coating in Ringer's solution by (a) optical microscope and (b) SEM.

Highlights for review:

- Microstructure of laser cladded Fe-based coating evolved with the amount of layers.
- With the increasing layer, COF and volume loss decrease firstly and then increase.
- COF and Volume loss of 2-layer coating are greatly lower than those of 316L SS.
- Fixed potentials of 100 mV and -600 mV are beneficial to reduce the COF.

Conflict of Interest and Authorship Conformation Form

Please check the following as appropriate:

- ✔ All authors have participated in (a) conception and design, or analysis and interpretation of the data; (b) drafting the article or revising it critically for important intellectual content; and (c) approval of the final version.
- ✔ This manuscript has not been submitted to, nor is under review at, another journal or other publishing venue.
- ✔ The authors have no affiliation with any organization with a direct or indirect financial interest in the subject matter discussed in the manuscript
- ✘ The following authors have affiliations with organizations with direct or indirect financial interest in the subject matter discussed in the manuscript:

Author's name	Affiliation